Available online at www.sciencedirect.com

SCIENCE DIRECT®

ELSEVIER

International Journal of Heat and Mass Transfer 47 (2004) 4327–4338

International Journal of HEAT and MASS TRANSFER

www.elsevier.com/locate/ijhmt

Heat transfer and fluid flow analysis in plate-fin and tube heat exchangers with a pair of block shape vortex generators

Jin-Sheng Leu [a], Ying-Hao Wu [b], Jiin-Yuh Jang [b,*]

[a] Department of Aircraft Engineering, Air Force Institute of Technology, Kaohsiung 82042, Taiwan
[b] Department of Mechanical Engineering, National Cheng-Kung University, Tainan 70101, Taiwan

Received 9 May 2003; received in revised form 23 April 2004
Available online 26 June 2004

Abstract

Numerical and experimental analyses were carried out to study the heat transfer and flow in the plate-fin and tube heat exchangers with inclined block shape vortex generators mounted behind the tubes. The effects of different span angles α ($\alpha = 30°$, $45°$ and $60°$) are investigated in detail for the Reynolds number ranging from 400 to 3000. Numerical simulation was performed by a 3D turbulence analysis of the heat transfer and fluid flow. Experiments were carried out by an infrared thermovision and a water tunnel system, respectively, to visualize the temperature distribution and local flow structure. The results indicated that the proposed heat transfer enhancement technique is able to generate longitudinal vortices and to improve the heat transfer performance in the wake regions. The case of $\alpha = 45°$ provides the best heat transfer augmentation. A reduction in fin area of 25% may be obtained if vortex generators embedded fins are used in place of plain fins at $Re_{\mathrm{Dh}} = 500$.

© 2004 Published by Elsevier Ltd.

Keywords: Vortex generator; Heat transfer enhancement; Plate-fin and tube heat exchanger

1. Introduction

Plate-finned-tube heat exchangers are one of the most used compact heat exchangers in automobiles, air-conditioners, and chemical industries. For typical applications, the airside resistance generally comprises over 90% of the total thermal resistance. Therefore, enhanced surfaces are often employed to effectively improve the airside heat transfer performance of the plate-fin and tube heat exchangers. One frequently used method for heat transfer enhancement employs surfaces that are interrupted periodically along the streamwise direction. Typically, these surfaces are in the form of wavy, louver, slit, or offset strip fins. Despite the fact that interrupted surfaces can significantly improve the heat transfer performance, the associated penalty of pressure drop is also tremendous. Another common method is to apply vortex generators (VG), such as ribs, wings and winglets. Vortex generators usually are incorporated into a surface by means of embossing, stamping, punching, or attachment process. They generate longitudinal vortices which swirl the primary flow and increase the mixing of downstream regions. In addition, the vortex generator determines the secondary flow pattern. Thus, heat transfer enhancement is associated with the secondary flow with relatively low penalty of pressure drop (Jacobi and Shah [1]).

The first literature reporting the enhancement of heat transfer of using surface protrusion vortex generators is by Edwards and Alker [2]. They noted a maximum increase in the local Nusselt number of 40%. Eibeck and Eaton [3] conducted heat transfer measurement for a single longitudinal vortex embedded in a turbulent boundary layer. They interpreted their data in terms of vortex circulation and boundary layer thickness. Pauley

---

[*] Corresponding author. Tel.: +886-6-2088573/2757575x 62148; fax: +886-6-2753850.

E-mail address: jangjim@mail.ncku.edu.tw (J.-Y. Jang).

0017-9310/$ - see front matter © 2004 Published by Elsevier Ltd.
doi:10.1016/j.ijheatmasstransfer.2004.04.031

Nomenclature

A	total surface area (m^2)
A_0	minimum free flow area (m^2)
C_p	dimensionless pressure coefficient
d	tube diameter (mm)
D_h	hydraulic diameter (mm)
f	fanning friction factor
$\bar{h}$	averaged heat transfer coefficient ($W\,m^{-2}\,°C^{-1}$)
j	Colburn factor, $j = \frac{h}{\rho u_{in} C_p} Pr^{2/3}$
k	turbulent kinetic energy ($m^2\,s^{-2}$)
k_s	conductivity of fin, ($W\,m^{-1}\,°C^{-1}$)
L	flow length, $L = 3X_L$ (mm)
Nu	local Nusselt number
$\overline{Nu}$	averaged Nusselt number
P	pressure (Pa)
Pr	Prandtl number
q''	heat flux ($W\,m^{-2}$)
Re	Reynolds number based on hydraulic diameter, $Re = U_{in}D_h/\nu$
S	fin spacing (mm)
T	temperature (°C)
T'	fluctuation temperature (°C)
T_b	bulk mean temperature (°C)
U_{in}	inlet frontal velocity ($m\,s^{-1}$)
u, v, w	velocity of air stream along x-, y-, z-coordinates ($m\,s^{-1}$)
X, Y, Z	dimensionless coordinates
x, y, z	coordinate (m)
X_L	tube longitudinal pitch (mm)
Greek symbols	
α	vortex generator span angle (degree)
ΔP	pressure drop (Pa)
ε	dissipation rate ($m^2\,s^{-3}$)
Θ	dimensionless temperature, $\Theta = (T - T_w)/(T_i - T_w)$
θ	dimensionless fluctuation temperature, $\theta = T'/(T_i - T_w)$
μ	dynamic viscosity (cp)
ρ	density ($kg\,m^{-3}$)

and Eaton [4] extended this work to consider vortex pairs. Co-rotating pairs were observed to move together and coalesce into a single vortex as they were advected downstream.

In recent years, the use of vortex generators in channel flow applications has received considerable attention. Tigglebeck et al. [5] and Fiebig et al. [6] used the delta wing, rectangular wing, delta winglet, and rectangular winglet as vortex generators and utilized liquid crystal thermograph to measure the local heat transfer coefficient. Their results identified an increase in the local heat transfer coefficient in the order of several hundred percent and a mean heat transfer enhancement of more than 50%. Biswas et al. [7] studied the flow structure of an air stream over winglet pair type vortex generators. They found that the winglet pair produced a main vortex, a corner vortex, and an induced vortex. The main vortex was formed by flow separation at the leading edge of the winglet, while the corner vortex was generated by the deformation of the near wall vortex lines at the pressure side of the winglet. Gentry and Jacobi [8] studied the interactions of delta-wing type vortex generators with the boundary layer on a flat plate. Their results identified a 50–60% enhancement of the average heat transfer. Sohankar and Davidson [9] analyzed three-dimensional unsteady laminar flow and heat transfer in a channel with a pair of inclined block shape vortex generators. They found unsteady flow occurred at $Re_H > 1000$. When the thickness and span angle are increased, stronger and bigger streamwise vortices are formed downstream of the vortex generators.

Fiebig et al. [10] and Valencia [11] considered the application of delta, rectangular, delta winglet, and rectangular winglet type vortex generators in fin-tube heat exchangers. These studies investigated various geometric parameters, including aspect ratio and angle of attack. It is shown that the ratio of heat transfer to flow loss was highest when a delta winglet vortex generator was used with an angle of attack of 30° and with an aspect ratio of 2. For the inline tube arrangement, the vortex generator increases the heat transfer coefficient by 55–65%, resulting in a corresponding increase of 20–45% in the apparent friction factor. Torii et al. [12] proposed a novel strategy that can augment heat transfer but nevertheless can reduce pressure-loss in fin-tube heat exchanger in a relative low Reynolds number flow, by deploying delta winglet-type vortex generators. In case of staggered tube banks, the heat transfer was increased by 10–30%, and yet the pressure loss was reduced by 34–55%. In the case of in-line tube banks, the heat transfer was augmented by 10–210% together with the pressure loss reduction of 8–15%. Wang et al. [13] utilized a dye-injection technique to visualize the flow structure for annular and delta winglet vortex generators. For the same winglet height, the delta winglet vortex generator shows more intensively vortical motion than that of annular vortex generator; while, the corresponding pressure drops of the delta winglet vortex generator are lower than those of annular vortex generator. Lin and Jang [14] numerically and experimentally studied the wave-type vortex generator in plate-fin and tube heat exchangers. Their study identifies a maximum improvement of 120% in the local heat transfer coefficient and an improvement of 18.5% in the average heat transfer coefficient.

The foregoing literature review shows that no related 3D numerical or experimental analysis for a pair of inclined blocks as vortex generator for a plate-fin and tube heat exchanger has been published. This has motivated the present investigation. The major parameters influencing the performance for a pair of inclined blocks as vortex generator are the position, size and span angles. However, the present investigation mainly aims to evaluate the effects of span angle α on the thermal-hydraulic characteristics. Three different span angles ($\alpha = 30°$, $45°$ and $60°$) are investigated in detail for the Reynolds number ranging from 400 to 3000. Turbulent numerical simulations for the three-dimensional fluid flow and heat transfer over a 3-row tube are performed, and the effect of turbulence is simulated by the k–ε extended turbulence model. The conjugated convective heat transfers in the flow field and heat conduction in the fins are also considered. In addition, experiments were carried out by an infrared thermovision and a water tunnel system, respectively.

2. Mathematical analysis

Fig. 1 presents the physical model and relevant geometrical dimensions in both the numerical and experimental studies for the plate-fin and tube heat exchanger with a pair of block shape vortex generators. Three

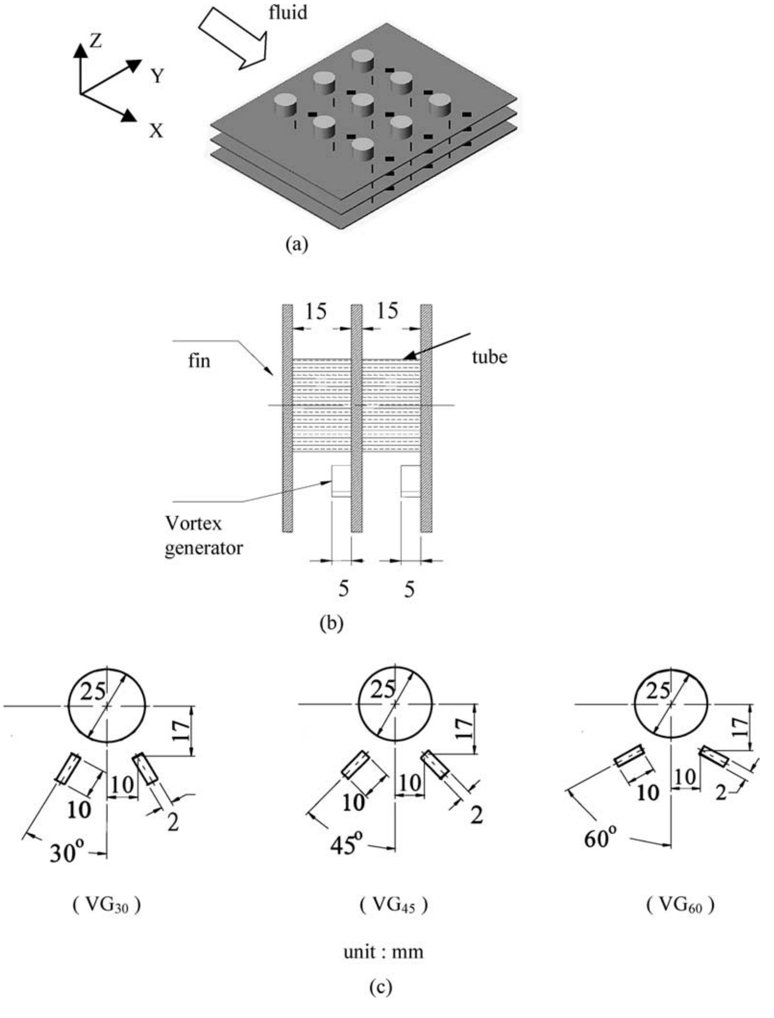

Fig. 1. Physical model and relevant geometrical dimensions of the vortex generators. (a) Physical model (top view), (b) side view, and (c) three different span angles.

different span angle α ($\alpha = 30°$, $45°$, and $60°$), relative to the main flow direction, were investigated in this study. The computational domain is shown in Fig. 2. The fluid is considered incompressible with constant properties and the flow is assumed to be turbulent, steady and no viscous dissipation. The dimensionless time averaged equations for continuity, momentum (Reynolds-averaged Navier–Stokes equations) and energy may be expressed in tensor form as:

$$\frac{\partial U_i}{\partial X_i} = 0 \tag{1}$$

$$\frac{\partial}{\partial X_j}(U_i U_j) = -\frac{\partial P}{\partial X_i} + \frac{1}{Re}[\nabla^2 U_i] - \frac{\partial}{\partial X_j}(\overline{u_i u_j}) \tag{2}$$

$$\frac{\partial}{\partial X_j}(\Theta U_j) = \frac{1}{Re\,Pr}[\nabla^2 \Theta] - \frac{\partial}{\partial X_j}(\overline{u_j \theta}) \tag{3}$$

In the above equations, the average velocity (U) and fluctuation velocity (u) have been nondimensionalized with the uniform inlet velocity u_{in} at the channel inlet, all length coordinates with the fin spacing S, and the pressure with ρu_{in}^2. The Reynolds number is defined as $Re = U_{\text{in}} D_{\text{h}}/\nu$, where $D_{\text{h}} = 4A_0L/A$ is the hydraulic diameter; A and A_0 are total surface area and minimum free flow area, respectively and L is the flow length defined as $3X_{\text{L}}$ in the present study (as shown in Fig. 2(a)). Eq. (2) contains Reynolds stresses that are modeled by the k–ε turbulence model proposed by Wang and Chen [15]. The velocity distribution in the near-wall region ($y^+ \leqslant 11.63$) is adopted the law of the wall given by Liakopoulos [16].

The heat conduction equation for the plate-fin region is expressed by:

$$\frac{\partial^2 \Theta_s}{\partial x_j^2} = 0 \tag{4}$$

The upstream boundary is established at a distance of one tube diameter in front of the leading edge of the fin.

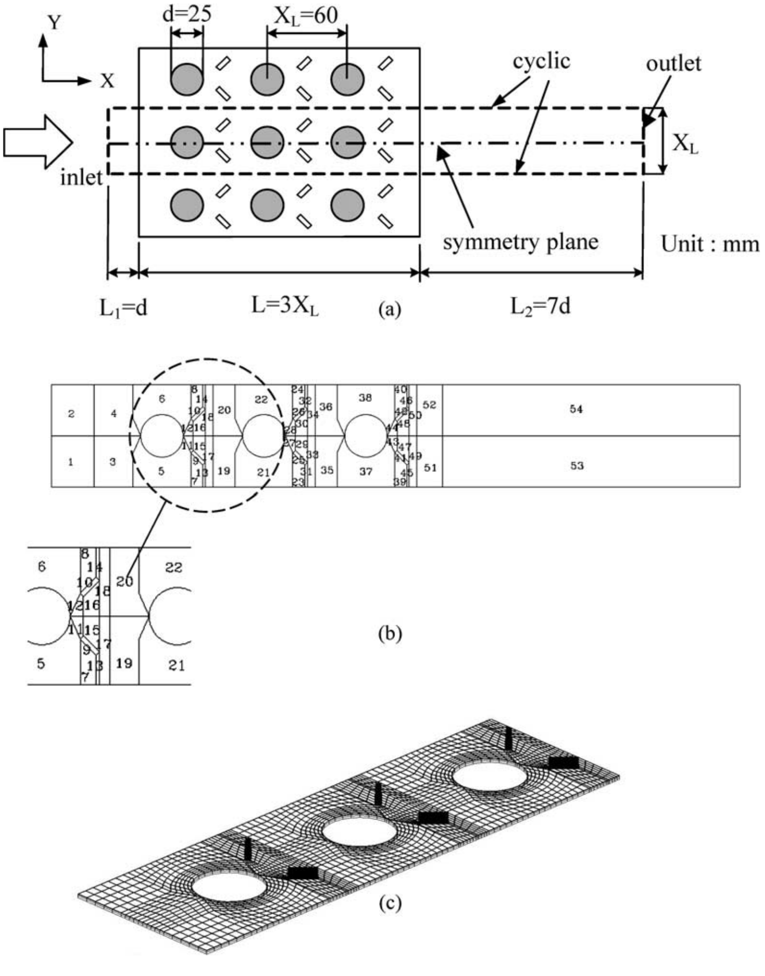

Fig. 2. The computational domain and grid systems. (a) Computational domain, (b) block partition and its numbers, and (c) solid fin region.

At this boundary, the flow velocity U_{in} is assumed to be uniform, and the temperature T_i is taken to be 20 °C. The intensity of the turbulence at the inlet is set to 3%. At the downstream end of the computational domain, located seven times the tube diameter from the last downstream row tube, streamwise gradient (Neumann boundary conditions) for all the variables are set to zero. At the solid surfaces, no-slip conditions and constant tube wall temperature T_{w} (70 °C) are specified. A cyclic match is established on the boundary planes (X–Y planes and X–Z planes). Additionally, at the solid–fluid interface, $T_{\text{s}} = T_{\text{fluid}}$; $-k_{\text{s}}\partial T_{\text{s}}/\partial n = -k_{\text{fluid}}\partial T_{\text{fluid}}/\partial n$.

The local Nusselt number is defined as follows:

$$Nu = D_{\text{h}}\frac{(-\partial T/\partial z)_{\text{vortex generator side}} + (-\partial T/\partial z)_{\text{plain surface}}}{(T - T_{\text{b}})_{\text{vortex generator side}} + (T - T_{\text{b}})_{\text{plain surface}}} \tag{5}$$

where T_{b} is the fluid bulk temperature, and is expressed as:

$$T_{\text{b}} = \frac{\int_{-S/2}^{S/2} UT\,\mathrm{d}z}{\int_{-S/2}^{S/2} U\,\mathrm{d}z} \tag{6}$$

The average Nusselt number, based on the primary and extended fin surfaces, is given by

$$\overline{Nu} = \frac{1}{L\cdot X_{\text{L}}}\int_0^L \int_{-X_{\text{L}}/2}^{X_{\text{L}}/2} D_{\text{h}} \times \frac{(-\partial T/\partial z)_{\text{vortex generator side}} + (-\partial T/\partial z)_{\text{plain surface}}}{(T - T_{\text{w}})_{\text{vortex generator side}} + (T - T_{\text{w}})_{\text{plain surface}}}\,\mathrm{d}y\,\mathrm{d}x \tag{7}$$

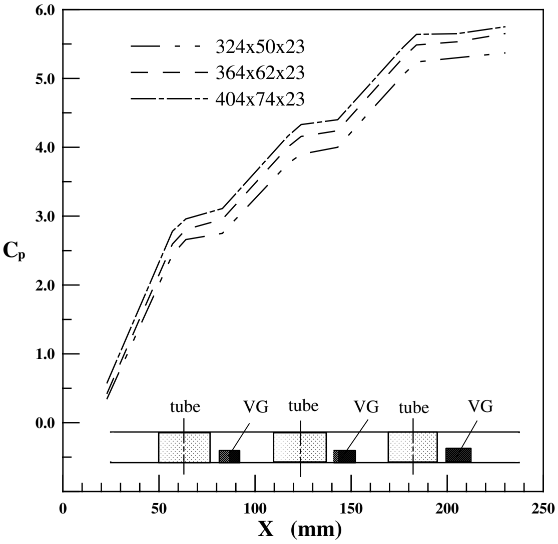

Fig. 3. Variations of C_p vs. streamwise direction X for three different grid systems.

The Fanning friction factor f and the Colburn factor j are defined as:

$$f = \frac{(p_{\text{in}} - p)}{\frac{1}{2}\rho u_{\text{in}}^2}\frac{D_{\text{h}}}{4L} = C_p\frac{D_{\text{h}}}{4L} \tag{8}$$

$$j = \frac{\overline{Nu}}{Re_{\text{Dh}}Pr^{1/3}} \tag{9}$$

where p_{in} is the pressure at the inlet and L is the flow length.

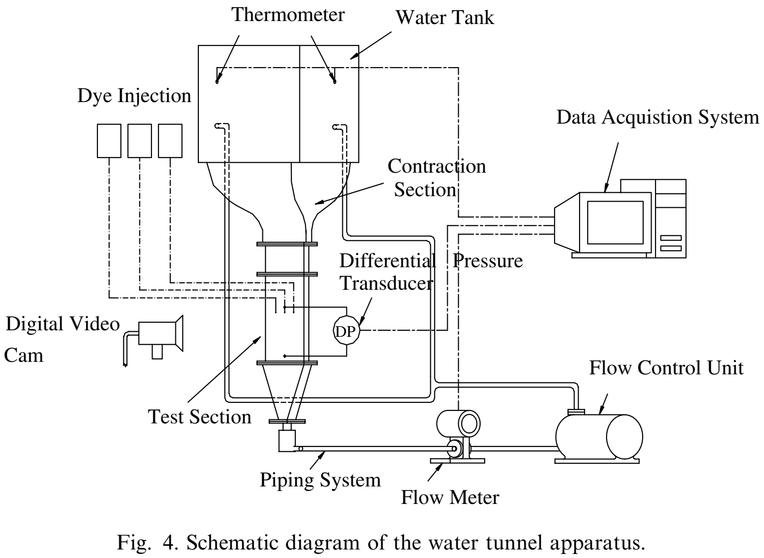

Fig. 4. Schematic diagram of the water tunnel apparatus.

3. Numerical method

The body-fitted coordinate along with multi-block system (54 blocks, see Fig. 2) was used first to generate a general curvilinear coordinate system by numerically solving Laplace equations. The governing equations are solved numerically using a finite difference formulation as described in detail in Patankar [17]. A third-order upwind total variable diminishing (TVD) scheme is used to model the convective terms of the governing equations, while second-order central difference schemes are employed for the viscous and source terms. A nonstaggered grid system of $364 \times 62 \times 23$ grid points is adopted typically in the computation domain. A careful check for the grid-independence of the numerical solutions has been made to ensure the accuracy and validity of the numerical results. For this purpose, three grid systems, $324 \times 50 \times 23$, $364 \times 62 \times 23$ and $404 \times 74 \times 23$, are tested. It is found that for $Re_{\mathrm{Dh}} = 1500$, the relative errors between the solutions of $364 \times 62 \times 23$ with the other two grid systems in the local dimensionless pressure coefficient C_p are within ±3% (as seen in Fig. 3). The convergence criterion is satisfied when the residuals of all variables are less than 1.0×10^{-4}. Computations were performed on P4-1.5G personal computer and CPU times were in the range of 20–24 h for each case.

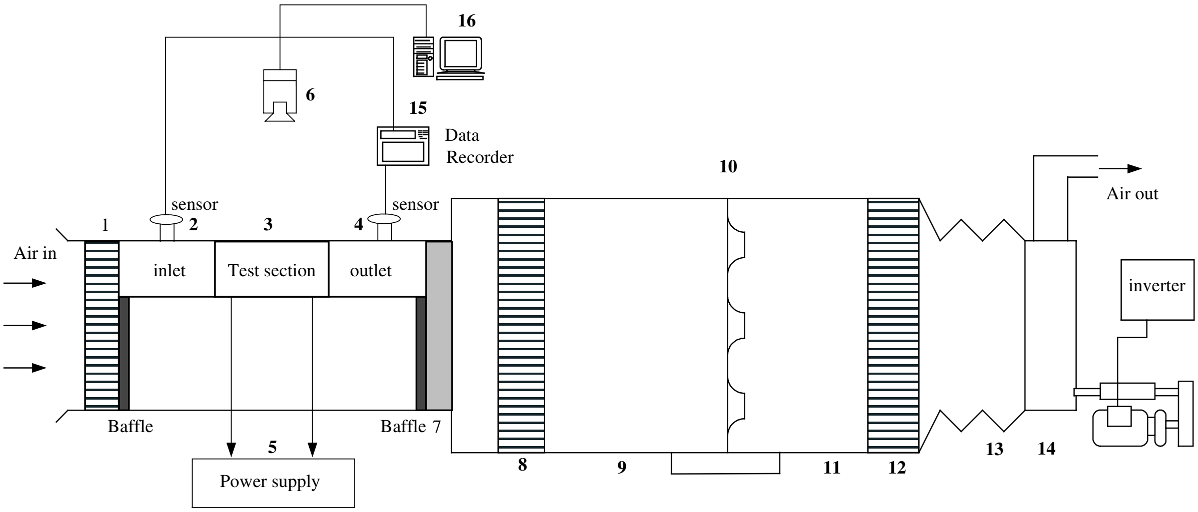

1.8.12.Flow Straightener
2.air side inlet temperature measuring section
3.test section
4.air side outlet temperature measuring section
5.power supply
6.infrared thermal imager
7.air mixer
9.nozzle pressure tap (inlet)
10.multi-nozzle plate
11.nozzle pressure tap (outlet)
13.flexible duct
14.variable exhaust fan system
15.data recorder
16.computer

Fig. 5. Schematic diagrams of experimental setup for infrared measurement system.

Table 1
Summary of estimated uncertainties

Primary and derived parameters	$U_{\mathrm{in}} = 0.46$ m/s $Re_{\mathrm{Dh}} = 500$		$U_{\mathrm{in}} = 2.78$ m/s $Re_{\mathrm{Dh}} = 3000$
Primary parameter (m_{a})	±2.0%		±1.0%
Primary parameter (m_{w})		0.002 L/s	
Primary parameter (T_{a})		±2.0%	
Primary parameter (ΔP)		0.1 Pa	
Primary parameter (T_{bulk})	±7.05%		±3.92%
Derived parameters (Re_{Dh})	±2.0%		±1.0%
Derived parameters (h)	±7.53%		±4.17%

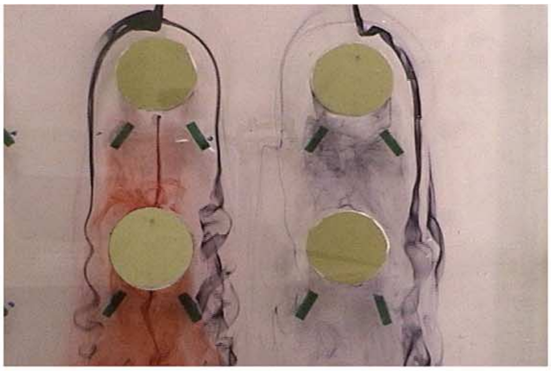

(a) VG$_{30}$

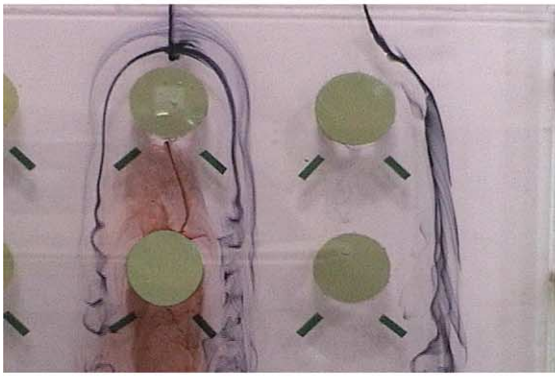

(b) VG$_{45}$

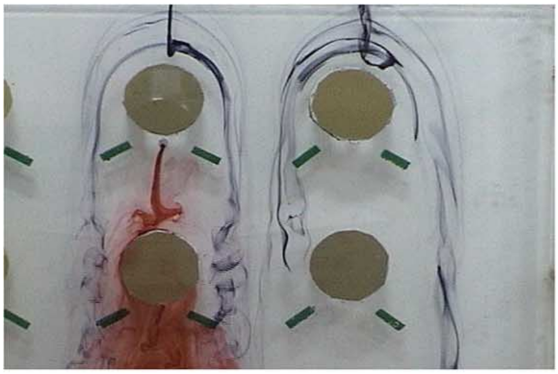

(c) VG$_{60}$

Fig. 6. Flow visualization for three different span angles α at $Re_{\mathrm{Dh}} = 500$.

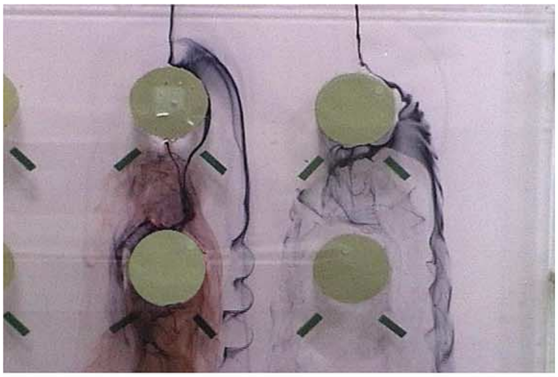

(a) $\mathrm{Re}_{\mathrm{Dh}}$=500

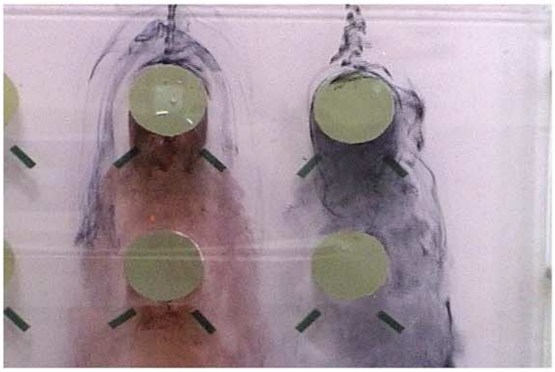

(b) $\mathrm{Re}_{\mathrm{Dh}}$=1500

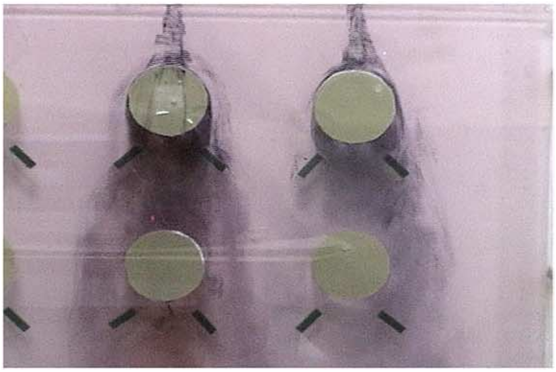

(c) $\mathrm{Re}_{\mathrm{Dh}}$=2500

Fig. 7. Flow visualization for span angle $\alpha = 45°$ at three different Re_{Dh}.

4. Experimental apparatus and methods

4.1. Water tunnel

Fig. 4 illustrates the water tunnel apparatus used to visualize the flow pattern. The water is powered by the boosted pump and is circulated in the tunnel system. The throttling valve behind the pump regulates the water flow rate. The test section was made of transparent acrylic and flow visualization was performed via a dye injection technique. Three needles that are capable of injecting color dyes are placed at the entrance of the inlet section. The injection ports can be either located in the center or near the wall to keep track of the trajectory

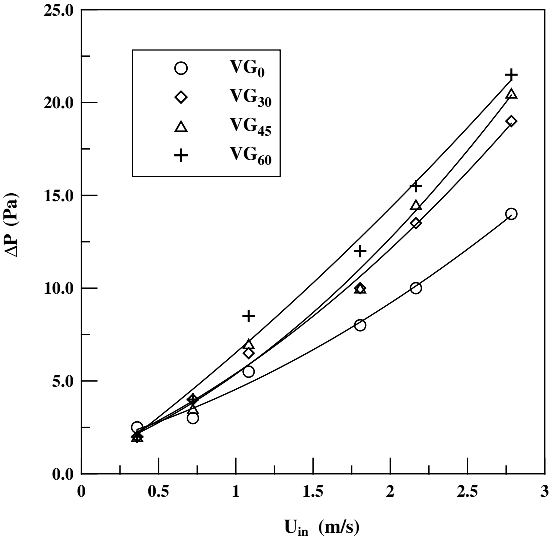

Fig. 8. The pressure drop ΔP vs. U_{in} for different span angles.

behavior. An additional dye injection port was placed at the rear of the acrylic tube to observe the flow motion of the wake region. The color in front of the test section is black whereas the color behind the tube is red. A digital video camera was placed outside the test section to record the trajectory of the injected dye. The water rate was measured by an accurate magnetic flow meter with a calibrated accuracy of 0.002 l/s. The pressure drop across the test section was measured by a precision pressure transducer with. resolution within 0.1% and reading to 0.1 Pa.

4.2. Infrared thermovision system

The infrared temperature measurement was carried out in an induced open wind tunnel as shown in Fig. 5. The airflow was driven by a 3.73 kW centrifugal fan with an inverter to provide various inlet velocities. A precision hot wire instrument SWEMAAIR 300 with air velocity probe SWA 31 was used to measure the inlet velocity. The accuracy for the present measuring range

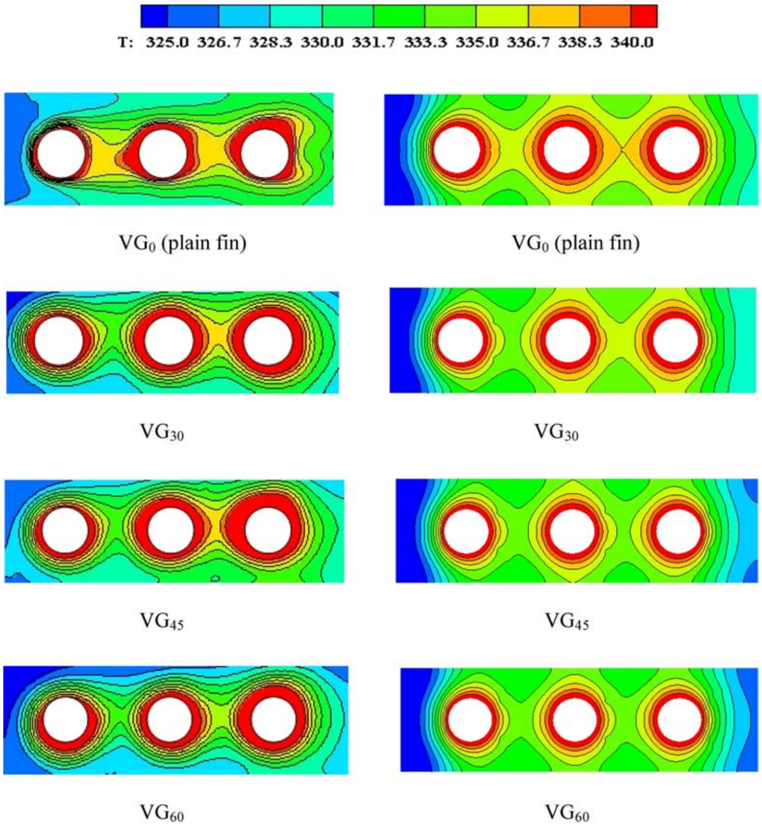

(a) experimental (b) numerical

Fig. 9. The isotherms on the fin surfaces for four test sections at $Re_{\text{Dh}} = 3000$, obtained by the infrared thermovision and by numerical simulation, respectively.

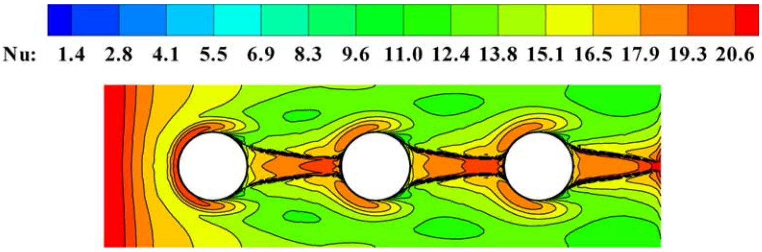

(a) VG_0

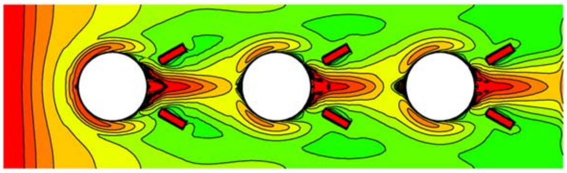

(b) VG_{30}

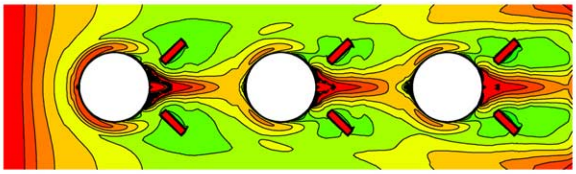

(c) VG_{45}

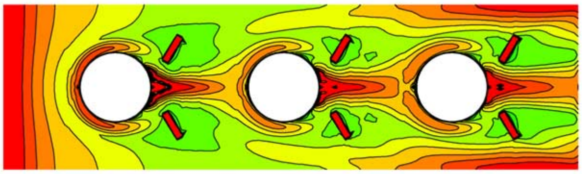

(d) VG_{60}

Fig. 10. Local Nu distribution across the fin surface at $Re_{\mathrm{Dh}} = 3000$.

of air velocity is ±3%. During the isothermal test, it was checked that the variations of the temperature in different locations were within ±0.2 °C and the free stream turbulence intensity of less than 3% was achieved. The air temperatures at the inlet and the exit zones across the test section were measured by 10 type-T thermocouples, pre-calibrated by a quartz thermometer to within 0.1 °C precision. The test samples are constructed of stainless steel. Each tube is heated locally by means of Joulean dissipation in a wire inserted in the central region of a cylinder installed within the tube. Electric power is supplied to the heater through cables from GW GPS-3303 multi-output DC power supply (0–30 V, 0–3 A). The surface of the fin is coated on both sides with a thin film of opaque paint with an emissivity (ε) of 0.95. In order to use an infrared camera to measure the temperature distribution on the surface of the plate-fin inside the test core, the top plate-fin of the test core is replaced with a transparent sheet of known transmissivity equal to 0.77.

Infrared thermal image was carried out using the NEC Thermo Tracer (TH7102MX). The sensing system comprises an uncooled focal plane array detector with image pixels of 320 (H) × 240 (V) elements. The infrared spectral band is 8–14 μm. The accuracy of TH7102MX is ±2%, the spatial resolution is 1.58 mrad, and the thermal sensitivity is less than 0.08 °C at 30 °C. The experimental procedure and data reduction were similar to those described in detail in Lin and Jang [14].

The estimated uncertainty is 2% for the fin surface temperature and 7% for the bulk mean temperature of the fluid. Using the method proposed by Kline and

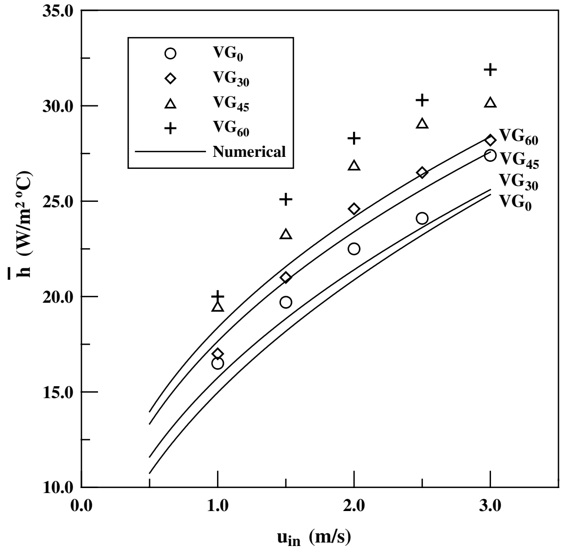

Fig. 11. The calculated and measured $\bar{h}$ vs. U_{in} for four test samples.

McClintock [18], the summary of the uncertainties is tabulated in Table 1.

5. Results and discussions

The close-up water flow visualization with the presence of vortex generators for three different span angles ($\alpha = 30°$, 45° and 60°) at $Re_{Dh} = 500$ are shown in Fig. 6(a)–(c). The dye injection position is placed near the wall. The color for the dye injection port in front of the 1st row tube is black, whereas the color behind the tube is red. It is seen that, from the black dye trajectory, the horseshoe vortex occurs in front of the tube and twists back a little and then swirls around the tube to the next tube row. An apparent pair of longitudinal vortices are formed downstream of the vortex generators. As the span angle α is increased, the strength of longitudinal vortex is intensified. It is interesting to note that the red dye is not constrained in the wake region, but directly flows downstream to the next tube row. Thus, the poor heat transfer characteristic behind the tube usually occurred for a plat-fin and tube heat exchanger can be improved with the present inclined block shape vortex generators. Fig. 7 shows the flow visualization for span angle $\alpha = 45°$ at three different Reynolds numbers ($Re_{Dh} = 500$, 1500, and 2500). The dye injection position is placed at the center of channel. One can see that the black dye travels around the tube, and then it divides into two streams. One passes over the inclined blocks and generates the longitudinal vortices; the other stream flows into the wake region and mixes the fluid in the recirculation zone (red dye). As the Reynolds number is increased, these effects are more pronounced. The measured pressure drops for three different span angles as a function of water inlet frontal velocity (0.5–3.0 m/s) are illustrated in Fig. 8. The corresponding pressure drop for the plain fin geometry (VG$_0$) is also shown for the comparison. As expected, VG$_{60}$ arrangement produces the largest pressure drop. One can see that as the velocity increases, the penalty of pressure drops (ΔP) of the proposed vortex generators relative to plain fin geometry is increased. For example, at $U_{in} = 1.0$ m/s, the ΔP of VG$_{60}$ is 33% larger than that of VG$_0$, while, at

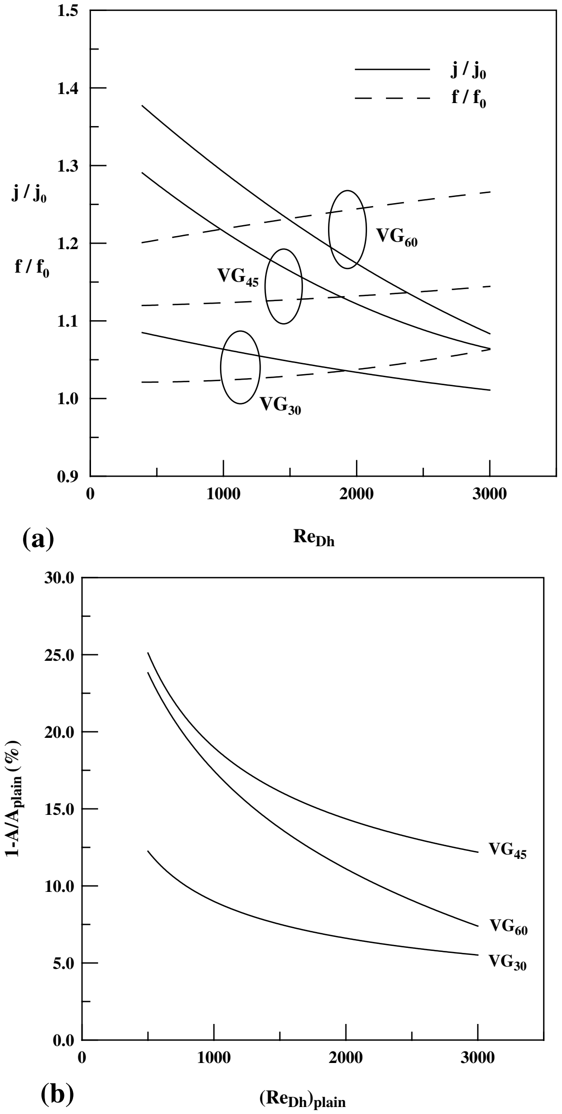

Fig. 12. (a) Variations of j/j_0 and f/f_0 vs. Re_{Dh} for different span angles. (b) The area reduction vs. $(Re_{Dh})_{plain}$ of using vortex generations relative to plain fin surfaces.

$U_{in} = 2.5$ m/s, the ΔP with inclined block shape vortex generator is 60% larger than that of plain fin surface.

Fig. 9(a) and (b) present the isotherms on the fin surfaces for four test sections (VG_0, VG_{30}, VG_{45} and VG_{60}), which are determined by the infrared thermovision and by numerical simulation, respectively. A comparison of the two sets of images shows that both methods indicate similar isotherms across the entire fin surface. It is observed that the temperature gradient between the tube rows gets larger as the span angle is increased. The local *Nu* number distributions of the fin surfaces for four test sections by numerical simulation are presented in the Fig. 10. When the vortex generator is employed, it leads the stream flow into the wake region and enhances the mixing of the hot and clod fluid, and then accelerates to hit the next tube. Thus, the local *Nu* number between the regions of vortex generators and tubes is greatly improved. The maximum improvement is seen to occur in the region behind the second row of tubes for the case of VG_{60}.

Fig. 11 presents the calculated and measured average heat transfer coefficient $\bar{h}$ at various inlet frontal velocities U_{in} ranging from 0.5 to 3 m/s for four test samples. Both the numerical and experimental results indicate that $\bar{h}$ is increased with increase of span angle α. For example, the $\bar{h}$ of VG_{60} is only 5–11% are larger than those of VG_{45}, while they are 7–18% and 21–29% larger than VG_{30} and VG_0, respectively. Furthermore, the numerical predictions underestimate the overall heat transfer coefficient. The discrepancy between the two sets of results is approximately 4–15%. This may be due to that fact that the experimental model considers all 3-tube rows, while the numerical computational domain was based upon the middle row of tubes only.

Fig. 12(a) illustrates the variations of j/j_0 and f/f_0 vs. Re_{Dh} for three different span angles. The j_0 and f_0 denote the Colburn factor and Fanning friction factors, respectively, for the plain-fin surface. As the span angle α is increased, both the j/j_0 and f/f_0 are increased. In addition, as the Re_{Dh} is increased, the j/j_0 is decreased, while the f/f_0 is increased. A close look at the figure indicates that, compared to the plain surface, the j for VG_{45} is increased by 8–30% across the *Re* range (400–3000), while the f is only increased by 11–15%. For VG_{60}, although the j is increased by 10–38%, the f is significantly increased by 20–27%.

The VG-1 (variable geometry) performance criteria, as described by Webb [19], represent the possibility of surface area reduction by using enhanced surfaces having fixed heat duty, temperature difference and pumping power. The possible area reduction, expressed as $1 - A/A_{plain}$ (where A and A_{plain} denote the surface areas of the vortex generators embedded fin and the plain fin, respectively), of using inclined block vortex generator with relative to the plain fin surfaces are presented in Fig. 12(b). It is shown that the VG_{45} arrangement gives the greatest area reduction ratio up to 25%. In addition, the area reduction ratio decreases as Re_{Dh} increases. Thus, the heat transfer enhancement by using inclined block vortex generator is more useful for low and moderate Reynolds number (e.g. $Re_{Dh} < 2000$).

6. Conclusion

Fluid flow and hear transfer over 3-row plate-fin and tube heat exchangers with and without a pair of inclined block shape vortex generators are studied numerically and experimentally. Flow is turbulent and three-dimensional and a whole computational domain (3 tube rows) from the fluid inlet to outlet is solved directly. The conjugated convective heat transfers in the flow field and heat conduction in the fins are considered also. The visual and numerical results demonstrate that this kind of vortex generators not only produce longitudinal vortices, but also aid the fluid into the wake re-circulation zone. As the span angle α is increased, the strength of the longitudinal vortex is intensified and both the Colburn and friction factors are increased. The VG_{45} arrangement provides the best relative heat transfer enhancement with 8–30% increase of Colburn factor across the *Re* range, while the Fanning friction factor is only increased by 11–15%, and it gives the greatest area reduction ratio up to 25%. In addition, the heat transfer enhancement by using inclined block vortex generator is more useful for low and moderate Reynolds numbers. Furthermore, the numerical predictions underestimate the overall heat transfer coefficient. The discrepancy between the two sets of results is approximately 4–15%.

Acknowledgements

Financial support for this work was provided by the National Science Council of Taiwan, under contract NSC 91-2212-E-269-008.

References

[1] A.M. Jacobi, R.K. Shah, Heat transfer surface enhancement through the use of longitudinal vortices: a review of recent progress, Exp. Therm. Fluid Sci. 11 (1995) 295–309.

[2] F.J. Edwards, G.J.R. Alker, The improvement of forces convection surface heat transfer using surfaces protrusions in the form of (A) cubes and (B) vortex generators, in: Proceedings of the 5th International Conference on Heat Transfer, Tokyo, vol. 2, 1974, pp. 244–248.

[3] P.A. Eibeck, J.K. Eaton, Heat transfer effects of a longitudinal vortex embedded in a turbulent boundary layer, ASME J. Heat Transfer 109 (1987) 37–57.

[4] W.R. Pauley, J.K. Eaton, Experimental study of the development of longitudinal vortex pairs embedded in a turbulent boundary layer, AIAA J. 26 (1988) 816–823.

[5] S.T. Tiggelbeck, N.K. Mitra, M. Fiebig, Experimental investigations of heat transfer enhancement and flow losses in a channel with double rows of longitudinal vortex generators, Int. J. Heat Mass Transfer 36 (1993) 2327–2337.

[6] M. Fiebig, H. Guntermann, N.K. Mitra, Numerical analysis of heat transfer and flow loss in a parallel plate heat exchanger element with longitudinal vortex generators as fins, ASME J. Heat Transfer 117 (1995) 1064–1067.

[7] G. Biswas, K. Torii, D. Fujii, K. Nishino, Numerical and experimental determination of flow structure and heat transfer effects of longitudinal vortices in channel flow, Int. J. Heat Mass Transfer 39 (1996) 3441–3451.

[8] M.C. Gentry, A.M. Jacobi, Heat transfer enhancement by delta-wing-generated tip vortices in flat-plate and developing channel flows, ASME J. Heat Transfer 124 (2002) 1158–1168.

[9] A. Sohankar, L. Davidson, Effect of inclined vortex generators on heat transfer enhancement in a three-dimensional channel, Numer. Heat Transfer, Part A 39 (2001) 433–448.

[10] M. Fiebig, A. Valencia, N.K. Mitra, Wing-type vortex generators for fin-and-tube heat exchangers, Exp. Therm. Fluid Sci. 7 (1993) 287–295.

[11] A. Valencia, M. Fiebig, N.K. Mitra, Heat transfer enhancement by longitudinal vortices in a fin-and-tube heat exchangers element with flat tubes, ASME J. Heat Transfer 118 (1996) 209–211.

[12] K. Torii, K.M. Kwak, K. Nishino, Heat transfer enhancement accompanying pressure-loss reduction with winglet-type vortex generators for fin-tube heat exchangers, Int. J. Heat Mass Transfer 45 (2002) 3795–3801.

[13] C.C. Wang, J. Lo, Y.T. Lin, C.S. Wei, Flow visualization of annular and delta winglet vortex generators in fin-and-tube heat exchanger application, Int. J. Heat Mass Transfer 45 (2002) 3803–3815.

[14] C.N. Lin, J.Y. Jang, Conjugate heat transfer and fluid flow analysis in fin-tube heat exchangers with wave-type vortex generators, J. Enhanc. Heat Transfer 9 (2002) 123–136.

[15] T.S. Wang, Y.S. Chen, Unified Navier–Stokes flow field and performance analysis of liquid rocket engines, AIAA J. 9 (5) (1993) 678–685.

[16] A. Liakopoulos, Explicit representation of the complete velocity profile in a turbulent boundary layer, AIAA J. 22 (1984) 844–846.

[17] S.V. Patankar, Numerical Heat Transfer and Fluid Flow, Hemisphere, New York, 1980.

[18] S.J. Kline, F.A. McClintock, Describing uncertainties single-sample experiments, ASME, Mech. Eng. 75 (1953) 3–8.

[19] R.L. Webb, Principles of Enhanced Heat Transfer, John Wiley & Sons, New York, 1994.